Biomass-Derived Nitrogen and Sulfur Co-Doped 3D Carbon Networks with Interconnected Meso-Microporous Structure for High-Performance Supercapacitors

Zhu Jiajia, *Hao Xiaodong*, *Wang Jie*, *Guo Hongshuai*,
Dou Hui, *Zhang Xiaogang* *

Jiangsu Key Laboratory of Electrochemical Energy Storage Technologies, College of Material Science and Engineering,
Nanjing University of Aeronautics and Astronautics, Nanjing 210016, P. R. China

(Received 12 June 2018; revised 25 July 2018; accepted 28 July 2018)

Abstract: Three-dimensional (3D) carbon networks have been explored as promising capacitive materials thanks to their unique structural features such as large ion-accessible surface area and interconnected porous networks, thus enhancing both ions and electrons transport. Here, sustainable bacterial cellulose (BC) is used both precursor and template for facile synthesis of free-standing N, S-codoped 3D carbon networks (a-NSC) by the pyrolysis and activation of polyrhodanine coated BC. The synthesized a-NSC shows highly conductive interconnected porous networks (24 S • cm^{-1}), large surface area (1 420 m^2 • g^{-1}) with hierarchical meso-microporosity, and high-level heteroatoms codoping (N: 3.1 % in atom, S: 3.2 % in atom). Benefitting from these, a-NSC as binder-free electrode exhibits an ultrahigh specific capacitance of 340 F • g^{-1} (24 μF • cm^{-2}) at the current density of 0.5 A • g^{-1} in 6 M KOH electrolyte, high-rate capability (71% at 20 A • g^{-1}) and excellent cycle stability. Furthermore, the assembled symmetrical supercapacitor displays a much short time constant of 0.35 s in 1 M $\mathrm{TEABF_4}$/AN electrolyte, obtaining a maximum energy density of 32.1 W • h • kg^{-1} at power density of 637 W • kg^{-1}. The in situ multi-heteroatoms doping enables biocellulose-derived carbon networks to exploit its full potentials in energy storage applications, which can be extended to other dimensional carbon nanostructures.

Key words: bacterial cellulose; 3D carbon networks; free-standing; N, S-codoping; supercapacitors

CLC number: O646 **Document code**: A **Article ID**: 1005-1120(2018)04-0590-13

0 Introduction

Electrochemical double-layer capacitors (EDLCs), also known as supercapacitors, store electrical energy at the electrode/electrolyte interface through reversible ion adsorption/ desorption[1-3]. Compared with rechargeable lithium batteries, EDLCs boast higher power density and longer lifespan[4]. However, the low energy density is a major barrier for the practical applications. Considerable efforts have been committed to developing high-capacitance electrode materials or broadening the cell voltage with different electrolytes that can enhance the energy density without sacrificing their existing advantages[5-7]. Porous carbons represent the most attractive class of EDLCs electrode materials owing to large specific surface areas (SSA), high electrical conductivity and chemical stability[8-10]. The commercial EDLCs are mainly constructed using activated carbon electrodes, but only with inferior rate capability because of the sluggish ion diffusion within tortuous microporosity[11]. Thus, engineering hierarchical meso-micropores structure is favorable. The mesopores supply fast ion-diffusion channels with improved rate capability,

---

* Corresponding author, E-mail address: azhangxg@nuaa.edu.cn.

How to cite this article: Zhu Jiajia, Hao Xiaodong, Wang Jie, et al. Biomass-derived nitrogen and sulfur co-doped 3D carbon networks with interconnected meso-microporous structure for high-performance supercapacitors[J]. Trans. Nanjing Univ. Aero. Astro., 2018,35(4):590-602.
http://dx.doi.org/10.16356/j.1005-1120.2018.04.590

whilst micropores contribute to abundant active sites for ion adsorption[12-13].

During the last decades, many efforts have been devoted to develop high-performance porous carbons for EDLCs. Especially, the design and preparation of 3D carbon networks assembled from nanofibers are highly desirable owing to their structural advantages as follows: (Ⅰ) interconnected continuous networks facilitate fast ion/electron transport along 3D directions and ensure structure-buffering space; (Ⅱ) 1D fiber structure possesses a high surface-to-volume ratio to increase the utilization of SSA for charge accommodation; and (Ⅲ) nanosized subunits guarantee sufficient contact areas between the electrolyte and active sites[14-16]. David et al. proposed an efficient strategy for carbonization of electrospun ZIF-8@PAN nanofibers to prepare 3D carbon networks, exhibiting a specific capacitance of 307 $F \cdot g^{-1}$ at 1 $A \cdot g^{-1}$ in H_2SO_4 electrolyte[17]. The interconnected graphene fibers were synthesized by hydrothermal treatment of graphene oxide ribbons and consequent laser irradiation[18]. The 3D graphene networks structure effectively eliminates the self-restacking of 2D graphene, maintaining fast axial/radial ion diffusion. Unfortunately, graphene or ZIF-derived carbons were used to construct 3D carbon networks, which usually involved expensive/complicated preparation processes and environmentally unfriendly[19-20]. From the viewpoint of practical application, it is highly desirable to develop a simple and cheap way for fabricating porous carbons in large scale. Currently, many researchers tend to fabricate carbon nanomaterial from biomass, which is low-cost, ecofriendly and easy fabrication[21-23]. Bacterial cellulose (BC), a typical biopolymer, can be obtained by an industrial-scale microbial fermentation process[24]. In terms of microstructure, BC has interconnected porous networks, which consist of random cellulose nanofibers with a diameter of 20—100 nm, thus providing high SSA and porosity[25]. Consequently, it can be an ideal platform for design of value-added carbon-based nanomaterials. Our group recently reported a silica-assisted method for fabrication of carbon nanofiber networks by confining nanospace pyrolysis of BC with a self-activation process[26]. Benefitting from its mesopores-dominated porosity and good conductivity, the as-prepared carbon films display excellent rate performance. Nevertheless, in situ release gas as activator only creates a limited SSA of 624 $m^2 \cdot g^{-1}$, leading to an inferior capacitance. The chemical activation has been intensively used to synthesize high-SSA porous carbons[27]. The hierarchical porous carbonaceous aerogels with a large SSA of 2 200 $m^2 \cdot g^{-1}$ were synthesized through KOH activation of renewable seaweed, achieving multiple energy storage[28].

The capacitance property could be further enhanced by the introduction of heteroatoms into the sp^2-hybridized carbon lattice[29]. It has been demonstrated that the incorporation of nitrogen (N) into carbon matrix could not only enhance the conductivity of carbon frameworks, but also significantly increase interface wettability of electrode/electrolyte and induce the additional pseudocapacitance[30-32]. The N-doped ordered mesoporous carbon was prepared by Ni-assisted chemical vapor deposition, manifesting a gravimetric capacitance as high as 855 $F \cdot g^{-1}$ at 1 $A \cdot g^{-1}$ and high-rate performance in aqueous electrolyte[30]. Similarly, doping sulfur (S) into carbon matrix also can decrease charge transfer resistance[33]. Compared to single-atom doping, codoping could take advantage of synergetic effects, thereby benefitting the overall electrochemical performance[34-36]. Qiao et al. revealed a synergistic performance enhancement of N and S dual-doping resulted from the redistribution of spin and charge densities by the experimental and theoretical calculations[34].

Guiding by these, we propose a facile and green route to prepare free-standing N, S-codoped 3D carbon networks by direct pyrolysis and activation of BC @ polyrhodanine nanocomposites. The polyrhodanine provides in situ codoping source for both N and S, derived from oxidation polymerization processes. The synthesized carbon nanofibers (a-NSC) present a large SSA with hierarchical meso-micropores structure, interconnected porous networks, high-level N, S-codoping and good electronic conductivity (24 S · cm^{-1}). With these features, a-NSC as binder-free EDLCs electrode achieves a remarkable specific capacitance and high-rate capability in aqueous electrolyte. Moreover, the assembled symmetric EDLCs obtain a high energy density and power density in organic electrolyte. This work offers a low-cost and green route for the design and large-scale preparation of high-performance porous carbons in the energy storage field.

1 Experiment

1.1 Materials synthesis

Polymerization of polyrhodanine on bacterial cellulose: $FeCl_3$ (30 mM) dissolved in 30 mL deionized water, followed by vigorous stirring for 1 h. The BC films were immersed into the well-dispersed oxidant solution and stirred slowly for 6 h at room temperature. The obtained BC-Fe (III) films were viscous, displaying a yellow color. Rhodanine monomers (50 mM) were dissolved in 50 mL of deionized water and heated to 60 °C under vigorous stirring to ensure the monomer dissolved completely. The BC-Fe (III) films were added into the prepared rhodanine monomers solution. The in situ oxidative polymerization of rhodanine with BC-Fe (III) was conducted at 60 ℃ for 24 h under magnetic stirring. Finally, the obtained nanocomposite, called as BC@PR, was washed with ethanol and distilled water and freeze-dried overnight.

Preparation of a-NSC, NSC and carbon nanofibers (CNF): The BC@PR was heated with the heating rate of 2 ℃ · min^{-1} to 400 ℃ for 1 h, and then with 5 ℃ · min^{-1} to 800 ℃ for 2 h under a flowing N_2 atmosphere, and was called NSC. The NSC and KOH were mixed and heated up with the heating rate of 5 ℃ · min^{-1} to 700 ℃ for 1 h in the N_2 atmosphere. The mass ratio of KOH to NSC was 1 ∶ 1. After activation, the products were washed thoroughly with HCl solution (1 M) and lots of distilled water for several times, and dried overnight at 70 ℃. The obtained carbons were denoted by a-NSC. For comparison, BC was direct pyrolyzed under the same condition of NSC, which was noted as CNF.

1.2 Characterizations

The morphologies of samples were characterized by field-emission scanning electron microscopy (SEM) and transmission electron microscopy (TEM) with a Hitachi S-4800I and FEI Tecnai G2F20, respectively. Thermogravimetric analysis was conducted on a TG-DSC instrument (NETZSCH STA 409 PC) under N_2 protection at heating rate of 10 ℃ · min^{-1} from 30 ℃ to 900 ℃. The N_2 adsorption/desorption technique was carried out using an ASAP 2020 accelerated surface area and porosimetry instrument (Micromeritics BK122T-Banalyzer), equipped with automated surface area, at 77 K using Brunauer-Emmett-Teller (BET) calculations for the surface area. The total pore volume and pore size distribution (PSD) were obtained from the adsorption isotherms using non-local density functional theory (NLDFT) model. The X-ray photoelectron spectroscopy (XPS) analysis was performed on a Perkin-Elmer PHI 550 spectrometer with Al K_α (1 486.6 eV) as the X-ray source. Raman spectra were conducted on the HORIBA Scientific LabRAM HR Raman spectrometer system with a 532.4 nm laser. Fourier transform infrared spectroscopy (FTIR) measurements were recorded on a Nicolet 750. Contact angles of samples were obtained on a video contact angle instrument (JC2000D7M). The electrical conductivity of sample was measured by a standard four-point probe system with a Kiethley 2700 multimeter.

1.3 Electrochemical measurements

All the electrochemical measurements were carried out on a CHI 660D electrochemical workstation. In the three-electrode system, a saturated calomel electrode (SCE) and a platinum plate electrode served as reference and counter electrodes, respectively. The free-standing carbon film (3 mg · cm^{-2}) with thickness of 100 μm was used as working electrode. No binder and additional conductive additive were added. The two symmetrical working electrodes were separated using membrane (GF/A, Whatman) soaked with electrolyte of 1-ethyl-3-methylimidazolium tetrafluoroborate (1 M $TEABF_4/AN$) in a 2016 type cell. The electrochemical impedance spectroscopy (EIS) measurements were performed at open circuit potential in the frequency range of 10^{-2} to 10^5 Hz at an AC amplitude of 5 mV. GCD cycles were tested using a LAND CT2001A electrochemical workstation.

In the three-electrode system, the specific capacitance of electrode calculated based on the discharge curves is according to the following equation

$$C=(I\Delta t)/(m\Delta V) \tag{1}$$

where I is the current loaded (A), Δt the discharge time (s), m the active material mass (g), and ΔV the potential window (V).

In the two-electrode system, the specific capacitance of the electrode was calculated from the discharge curve as

$$C_s=(4I\Delta t)/(m\Delta V) \tag{2}$$

where I is the current loaded (A), Δt the discharge time (s), m the total mass for both carbon electrodes (g), and ΔV the potential window (V).

The gravimetric energy density E and power density P against two electrodes in device was calculated as

$$E=CV^2/2 \tag{3}$$

$$P=E/\Delta t \tag{4}$$

where C is the capacitance of the symmetric EDLC (based on the total mass of electroactive materials in two electrodes), V the operating voltage (deduct the voltage drop), and Δt the discharge time (s).

2 Results and Discussion

The preparation processes for free-standing N, S-codoped carbon are schematically illustrated in Fig. 1(a). The pristine BC pellicle exhibits a gel-like and water-rich macroscopic morphology. The BC was used as template and coated with polyrhodanine (PR) to form the BC@PR nanocomposite with a chemical oxidation polymerization process. Typically, rhodanine monomer fully infiltrates into the 3D networks of BC along the nanofibers through the strong hydrogen bonding. Polymerization of rhodanine onto the surface of BC was induced using Fe(III) ion as the initiator and oxidant. The Fe(III) ion adsorbed on the porous surface of negatively charged BC driven by electrostatic interaction. After carbonization and further KOH activation, a porous N, S-codoped carbon (a-NSC) film was obtained. For comparison, pristine BC-derived carbon nanofibers (CNF) and N, S-codoped carbon (NSC) without activation were synthesized in the same way.

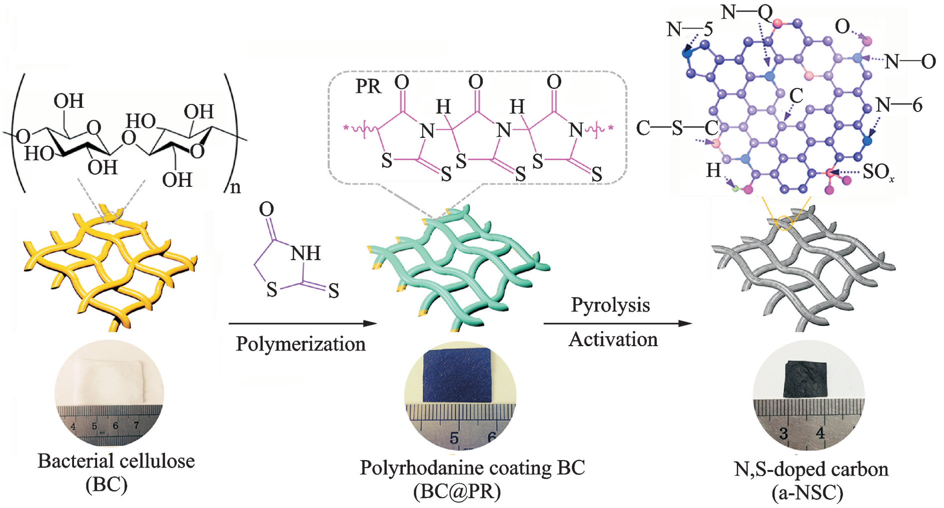

(a) The schematic illustration for fabricating free-standing N, S-codoped carbon with corresponding digital photographs

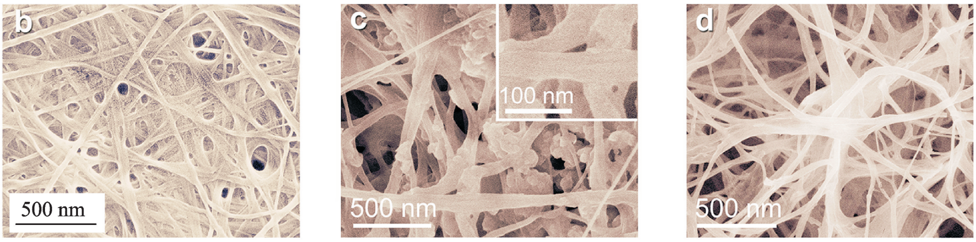

(b) BC pellicle (c) BC@PR pellicle (d) a-NSC

Fig. 1 The schematic illustration for fabricating free-standing N, S-codoped carbon with corresponding digital photographs and SEM images of BC pellicle, BC@PR pellicle and a-NSC

As revealed in scanning electron microscopy (SEM) images, BC@PR maintains 3D networks architecture with randomly coadjacent nanofibers of pristine BC (Figs. 1(b—c)), displaying a relatively rough surface after the PR coating. After pyrolysis and activation, the resulting a-NSC inherits the structural characteristics of 3D interconnected nanofibrous networks with a slight shrinkage of the frameworks (Fig. 1(d)). The diameter of carbon nanofibers is 20—50 nm, as determined by the transmission electron microscopy (TEM) image (Fig. 2(a)). And CNF and NSC also preserve an analogous morphology. Notably, the unique interconnected porous networks not only provide a large interfacial area for charge accommodation but also accelerate ion diffusion/electron transfer along 3D directions[37]. As observed from high-resolution TEM (Fig. 2(b)), a-NSC mainly consists of relatively disordered structure and partial orientated graphitic layers (002) with an interlayer spacing of about 0. 34 nm, which is beneficial to enhance electrical conductivity of carbon materials[38]. X-ray diffraction (XRD) further verifies the structure of CNF, NSC and a-NSC. To a-NSC, two broadened diffraction peaks locating at 24° (002) and 44° (100) imply dominant features of amorphous carbon, which is well-matching the TEM observations[38]. Moreover, there are no other perks (apart from 24° (002) and 44° (100)) which can be observed in the XRD. This case proves that CNF, NSC and a-NSC are pure carbon materials. Typical elemental mapping images of a-NSC (Fig. 2(c)) confirmed that homogeneous incorporation of N and S elements into the entire carbon networks.

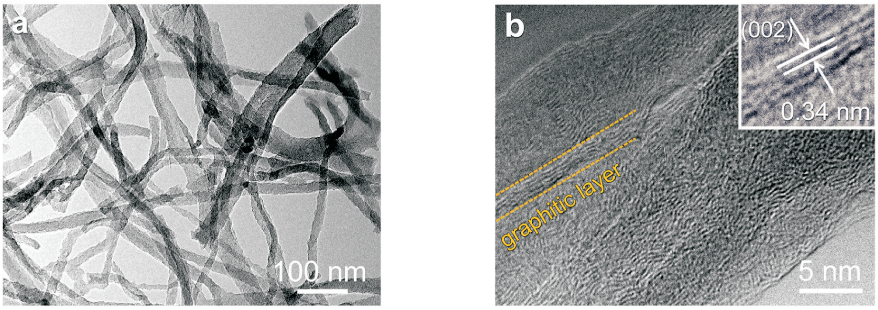

(a) TEM image of a-NSC (b) HRTEM image of a-NSC

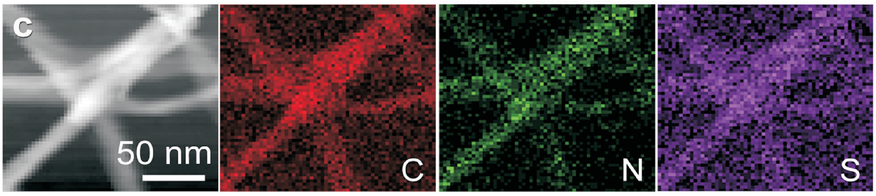

(c) Scanning TEM image of a-NSC and corresponding elemental mapping images of C, N, S

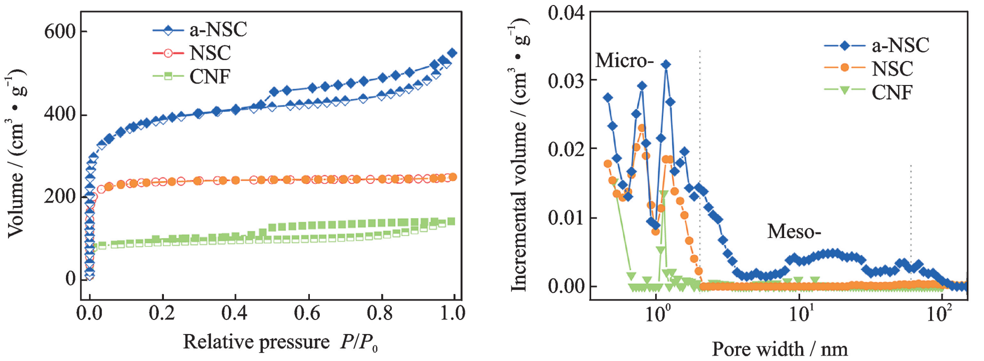

(d) N2 adsorption/desorption isotherms (e) Corresponding PSDs of a-NSC, NSC and CNF

Fig. 2 TEM image of a-NSC, HRTEM image of a-NSC (inset: the magnifed graphitic layers), scanning TEM image of a-NSC and corresponding elemental mapping images of C, N, S, N_2 adsorption/desorption isotherms and the corresponding PSDs of a-NSC, NSC and CNF.

The functional groups of samples were characterized by Fourier transform infrared spectroscopy (FTIR) spectra. The main characteristic peaks of BC at around 1 150 cm^{-1} (C═O), 2 950/1 450 cm^{-1} (C—H) and 3 450 cm^{-1} (O—H) were observed[39]. The BC@PR displays similar absorption peaks but with lower intensity. Simultaneously, the emerging peaks of C—S (637 cm^{-1}), C═S (1 240 cm^{-1}), C—N (1 380 cm^{-1}) and C═O (1 710 cm^{-1}) contributed by PR[37], manifesting that BC was successfully coated with PR. Thermogravimetric analyses (TGA) were used to investigate the carbonization process. Both BC@PR and BC mainly decomposed below 400 ℃ along with the release of gases (H_2O, CO_2), resulting in the formation of many pores. The residual mass of about 28.5% and 10.8% was obtained at 800 ℃ for BC@PR and BC, respectively.

The pore characterization of carbon networks was investigated by the N_2 adsorption/ desorption experiments. The a-NSC exhibits a hybrid I/IV-type isotherm curve with a distinct hysteresis loop of type H4 in the medium/high pressure region ($0.4 < P/P_0 < 1$), indicating existence of mesopores (Fig. 2(d)). It is clear that the significantly high uptake of a-NSC at low pressure region ($P/P_0 < 0.1$) is indicative for the abundant microporosity. The Brunauer Emmett Teller (BET) SSA of a-NSC is calculated to be 1 420 $m^2 \cdot g^{-1}$ with a total pore volume of 0.848 $cm^3 \cdot g^{-1}$ (Table 1), which is larger than that of NSC (934 $m^2 \cdot g^{-1}$, 0.359 $cm^3 \cdot g^{-1}$) and CNF (302 $m^2 \cdot g^{-1}$, 0.218 $cm^3 \cdot g^{-1}$). The increased SSA and pore volume can be attributed to KOH activation and heteroatoms doping. The pore size distribution (PSD) is further verified by the NLDFT analysis on the adsorption isotherm as shown in Fig. 2(e). As compared to microporous distribution of NSC, a reasonable meso-microporous dominant PSD was observed in a-NSC. Furthermore, for a-NSC, notable feature of high ratio of micropore volume to total volume up to 63% was noticed. The integration of large SSA and hierarchical meso-microporosity is extremely favorable for charge accumulation and rapid diffusion of ions[2, 11].

Table 1 BET surface area, pore structure parameters, conductivity tests and XPS elemental analysis of carbon materials

Samples	$S_{BET}^{(a)}$/ ($m^2 \cdot g^{-1}$)	Micro-S_{BET}/ ($m^2 \cdot g^{-1}$)	$V_{total}^{(b)}$/ ($cm^3 \cdot g^{-1}$)	Micro-V_{total}/ ($cm^3 \cdot g^{-1}$)	Conductivity/ ($S \cdot cm^{-1}$)	Elemental analysis/% (in atom)			
						C	N	S	O
CNF	302	250	0.218	0.118	1.2	87.1	—	—	12.9
NSC	934	914	0.359	0.350	31	85.5	2.3	5.4	6.8
a-NSC	1 420	1 060	0.848	0.539	24	79.4	3.1	3.2	14.3

Note: (a) Specific surface area determined according to BET method; (b) Total pore volume.

The chemical composition of codoped carbon was investigated by X-ray photoelectron spectroscopy (XPS). In survey spectra, both a-NSC and NSC exhibit typical N 1s, S 2s and S 2p peaks along with C 1s and O 1s, indicating effective doping of N and S into carbon lattice. The codoping level of two elements in a-NSC, N and S, reaches 3.1 % in atom and 3.2 % in atom, respectively (Table 1). Note that KOH treatment leads to an increase in oxygen content. The high-resolution C 1s spectrum for a-NSC (Fig. 3(a)) can be fitted to four subpeaks at around 284.5, 286.3, 288.2 and 290.1 eV, which corresponds to C=C/C—C, C—O, C=O and O=C—O, respectively[37]. The percentage of C=C/C—C was up to 81%, implying high graphitization degree[40]. In addition, high-resolution N 1s spectrum of a-NSC (Fig. 3(b)) reveals the existence of pyridinic N (N—6, 398.6 eV), pyrrolic N (N—5, 400.1 eV), graphitic N (N—Q, 401.1 eV) and pyridine-N-oxide (N—O, 403.2 eV)[41]. The N—6 (42.8%) and N—5 (13.6%) are able to enhance the capacitance due to their pseudo-capacity contributions, and N—Q (40.2%) can decrease intrinsic resistance of carbon electrode and facilitate electron transfer[11, 29, 42]. Moreover, the deconvoluted spectrum of S 2p (Fig. 3(c)) suggests that the binding states of sulfur are carbon-bonded thiophene-type sulfur (C—S—C: 164.0 eV for S 2p$_{3/2}$, 165.2 eV for S 2p$_{1/2}$) and highly oxidized sulfur species (SO$_x$, 168.2 eV)[41]. The dominated C—S—C (86%) plays a significant role in modifying the conductivity of carbon material[43]. The electrical conductivity of a-NSC and NSC was estimated to be 24 and 31 S • cm^{-1} (Table 1), respectively, measured by a four-probe method, which is far higher than that of undoped CNF (1.2 S • cm^{-1}). Significantly, surface functionalities also can enhance wettability of carbon electrode for electrolyte[29]. It was confirmed by the contact angle tests that a-NSC and NSC has more superior electrolyte wettability than CNF, easily allowing ions permeation into microporosity structure of electrode. The structural characterizations of samples were further confirmed Raman spectra (Fig. 3(d)). The ratios of

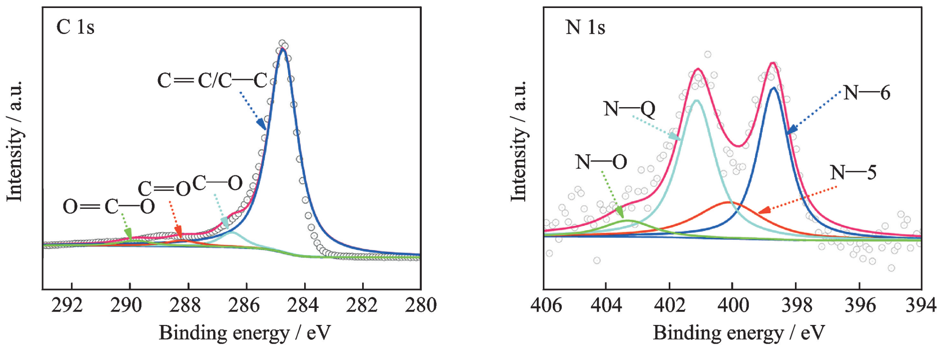

(a) High-resolution C 1s spectrum of a-NSC (b) High-resolution N 1s spectrum of a-NSC

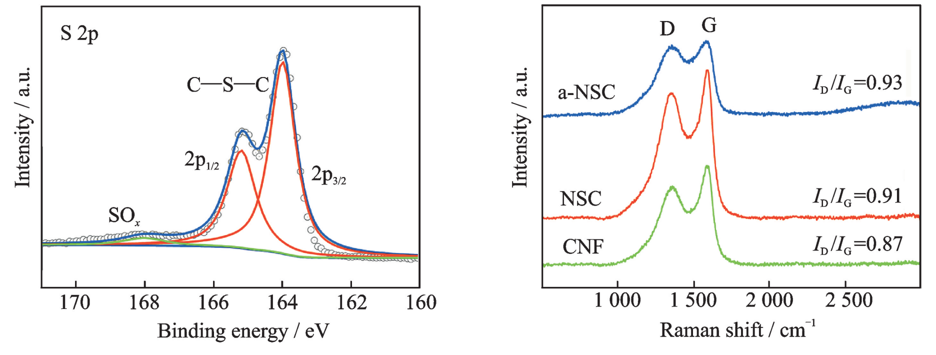

(c) High-resoulution S 2p spectrum of a-NSC (d) Raman spectra of a-NSC, NSC and CNF

Fig. 3 High-resolution C 1s spectrum of a-NSC, high-resolution N 1s spectrum of a-NSC, high-resolution S 2p spectrum of a-NSC, and Raman spectra of a-NSC, NSC and CNF

D band (disordered/defect carbon, 1 350 cm^{-1}) to G band (graphitic carbon, 1 580 cm^{-1}), calculated by the integrated areas, are higher for a-NSC and NSC than CNF (I_D/I_G: 0.93 and 0.91 vs 0.87), suggesting the presence of more defects created by the N, S-codoping and KOH activation[38, 42].

The as-prepared a-NSC features unique characteristics such as large SSA with hierarchical porosity, interconnected 3D networks morphology and N, S-codoping, which make it an ideal candidate for EDLCs. To investigate capacitive properties, a three-electrode configuration was fabricated with 6M KOH as electrolyte, and carbon film was directly used as binder-free working electrode. As shown in Fig. 4(a), both cyclic voltammetry (CV) plots of a-NSC, NSC and CNF display nearly symmetrical rectangular shapes at the scan rate of 10 mV · s^{-1}, demonstrating the formation of ideal electric double-layer (EDL). And the codoped carbon electrodes also showed some redox hump peaks, indicating the pseudocapacitive contribution from N doping. Apparently, the area of CV plot for a-NSC is much larger than the NSC and CNF, suggesting a better EDL behavior. As increasing the scan rate to 200 mV · s^{-1}, a-NSC still keeps a rather good rectangular-like shape. Galvanostatic charge/discharge (GCD) curves of the a-NSC show highly symmetry and nearly linear slopes at different current densities. Comparing with NSC and CNF, a larger discharge time was observed for a-NSC (Fig. 4(b)), suggesting a higher capacitance. The specific capacitances were calculated according the discharge of GCD curves (Fig. 4(c)). The a-NSC possesses a high specific capacitance of 340 F · g^{-1} at the current density 0.5 A · g^{-1} with superior rate capability of 240 F · g^{-1} at 20 A · g^{-1} (71%), which is much higher than that of the NSC (254 F · g^{-1} at 0.5 A · g^{-1}, 66% at 20 A · g^{-1}), CNF (219 F · g^{-1} at 0.5 A · g^{-1}, 50% at 20 A · g^{-1}), and most other BC-derived carbons for EDLCs applications. Apparently, the enhanced micropore SSA and N, S-functionalization upon doping improve the rate performance and capacitance of NSC electrode; further activation

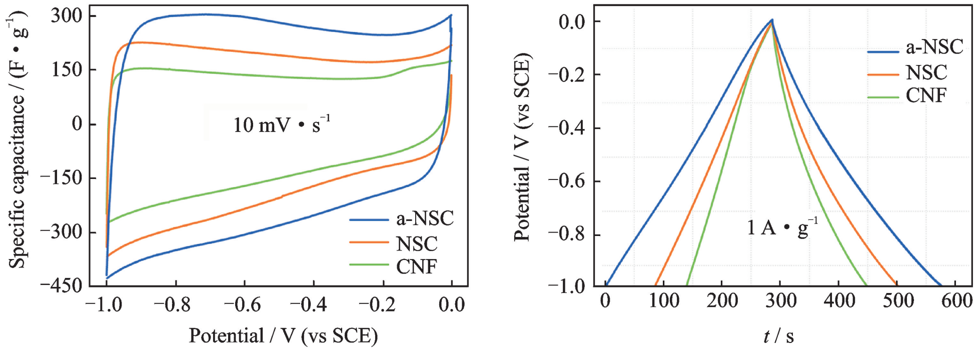

(a) CV plots of a-NSC, NSC and CNF electrodes at a scan rate of 10 mV • s^{-1}

(b) GCD curves of a-NSC, NSC and CNF electrodes at the current density of 1 A • g^{-1}

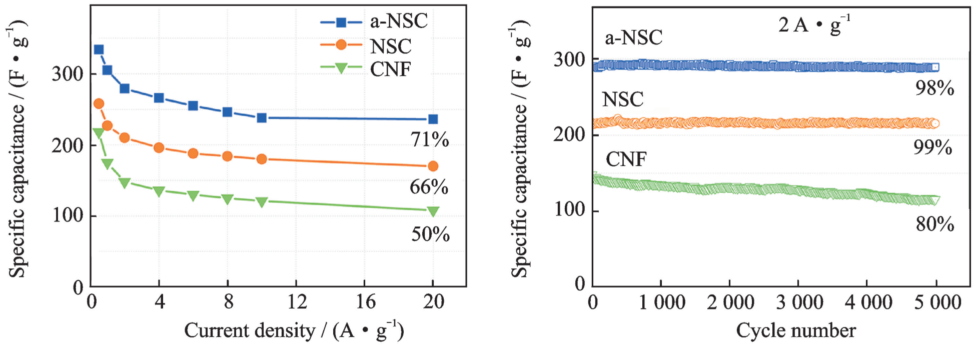

(c) Specific capacitance of a-NSC, NSC and CNF electrodes at different current densities

(d) Cycling stability of a-NSC, NSC and CNF electrodes

Fig. 4 Electrochemical performances using 6 M KOH as electrolyte in a three-electrode configuration achieved a large SSA with hierarchical meso-microporosity, ensuring the high capacitance and excellent rate characteristic of a-NSC electrode. The BET area-normalized capacitance of a-NSC can achieve a maximum of 24 μF • cm^{-2}. The improved ion-transport kinetics of electrodes were evidenced by electrochemical impedance spectroscopic (EIS) over a frequency range from 100 kHz to 10 MHz. a-NSC shows a smaller diameter of the semicircle in high-frequency ranges and shorter Warburg region with typical 45° slope than NSC and CNF, proving excellent ion diffusion/charge transfer process. And nearly vertical plot in low-frequency ranges suggests the good accessibility of electrolyte ions into porous carbon. The cycling performance of electrodes were evaluated by 5 000 GCD cycles at 2 A • g^{-1} at 6 M KOH electrolyte in Fig. 4(d). Both a-NSC and NSC exhibit high stability with 98% and 99% capacitance retention, respectively, which is far superior to the CNF (80%).

Such excellent capacitive performance can be attributed to unique structural advantages. Firstly, large SSA guarantees sufficient active sites for charge storage and hierarchical porosity can accelerate ion accumulation/diffusion, thus improving both capacitance and rate capability; secondly, interconnected 3D networks can construct conducting backbones for fast electron transfer and also provide multiple channels for the migration of ions. Moreover, the better wettability and conductivity owing to N, S-codoping further enhance the ion-accessible surface area and facilitate electron transport, and N—Q incorporated into the graphitic carbon plane (aromaticity C—N framework) can enhance the electrical conductivity of carbon electrode, significantly increasing the capacitance and rate capability. The presence of N—6 and N—5 (electrochemically active) also can introduce pseudocapacitance in the alkaline aqueous solution through the following faradaic reactions[11]

$$^*CH{-}NH_2+2OH^- \rightleftharpoons {}^*C{=}NH+2H_2O+2e$$

$$^*C{-}NH_2+2OH^- \rightleftharpoons {}^*C{-}NHOH+H_2O+2e$$

where $^*C$ stands for the carbon network.

To further evaluate supercapacitor performances, we constructed a symmetrical EDLCs cell of a-NSC in 1M tetraethylammonium tetrafluoroborate ($TEABF_4$) in acetonitrile (AN) with a wide voltage range of 0—2. 5 V. Both quasi-rectangle CV plots with scanning rates increasing from 20 to 500 mV • s^{-1}(Fig. 5(a)) and the symmetry and linear GCD curves even at a high current density of 20 A • g^{-1}(Fig. 5(b)), suggesting an ideal EDL behavior. The high specific capacitance of 148 F • g^{-1} for a-NSC is obtained from the GCD curve at 0. 5 A • g^{-1} (Fig. 5(c)). Increasing current density up to 20 A • g^{-1}, the capacitance maintains 100 F • g^{-1}, indicating high rate capability. The great performances can be ascribed to large ion-accessible surface area and optimized pore structure. As NLDFT analysis above (Fig. 2(e)), the meso-microporous PSD is effective for ions accumulation/transport in the $TEABF_4$/AN system (size: solvated TEA^+ of 1. 30 nm and solvated BF_4^- of 1. 16 nm)[7]. The interconnected porous networks also provide short ion-transport pathways. The Nyquist plot (Fig. 5(d)) shows a vertical curve at low-frequency region, indicating a nearly ideal capacitive behaviour. The high-frequency region for porous electrode is typically divided into two ranges by the knee frequency (265 Hz): The critical frequency at which all SSA is accessed, meaning that total EDL capacitance is reached. The a-NSC exhibits a frequency of 2. 86 Hz at a phase angle of −45° corresponding to a time constant of 0. 35 s (Fig. 5(e)). The high knee frequency and much short time constant induced by the good accessibility of the ions into 3D porous networks demonstrate the excellent power capability of the device. The Ragone plot for symmetrical EDLCs of a-NSC depicts that the energy density is about 32. 1 W • h • kg^{-1} at power density of 637 W • kg^{-1}, while the energy remains as high as 21. 7 W • h • kg^{-1} at power density of 28. 8 kW • kg^{-1} (Fig. 5(f)), which are significantly higher than symmetrical EDLCs of a-NSC in aqueous electrolyte and other carbon materials synthesized from biomass[26, 36, 44-48]. There is an excellent circulation with 94% retention after 10 000 cycles at 2 A·g^{-1} in 1 M $TEABF_4$/AN electrolyte, benefiting from excellent ion/electron transport during the long-term cycling.

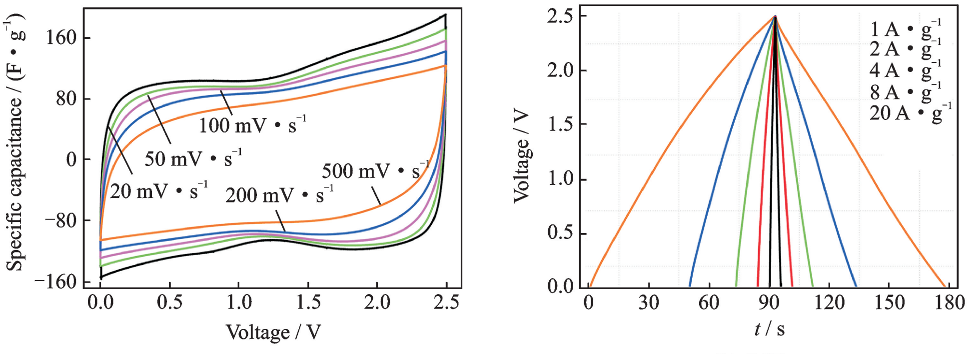

(a) CV plots (b) GCD curves

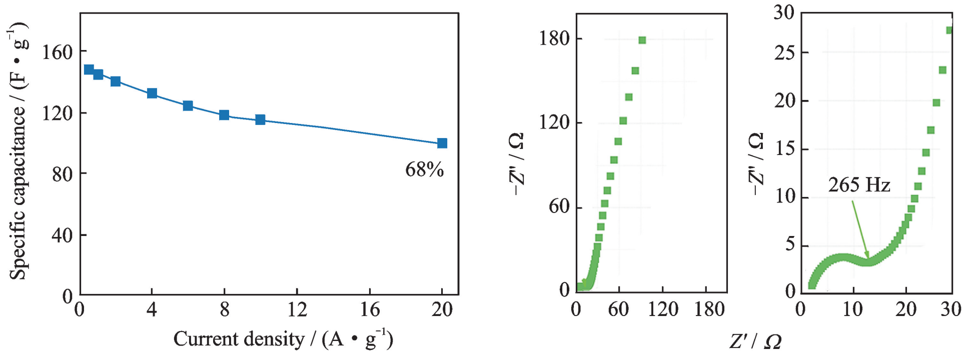

(c) Specific capacitance versus current density (d) Nyquist plot

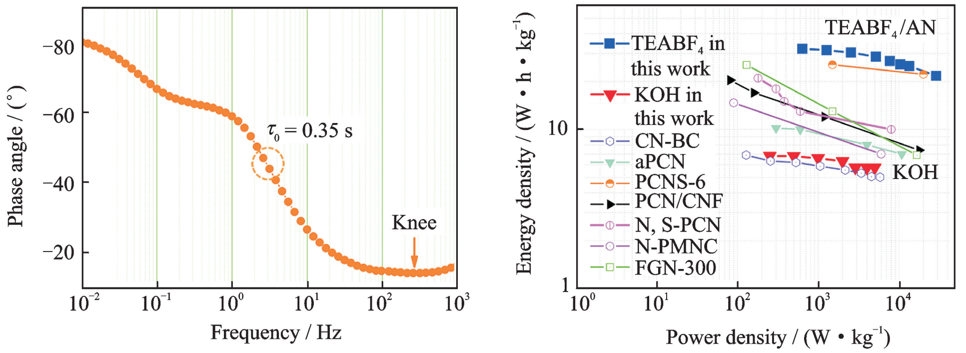

(e) Bode plot of phase angle versus frequency (f) Ragone plot for a-NSC in comparison with other carbon materials

Fig. 5 Symmetrical EDLCs performance of a-NSC using 1 M $TEABF_4$/AN as electrolyte, CV plots, GCD curves, specific capacitance versus current density, nyquist plot, bode plot of phase angle versus frequency, ragone plot for a-NSC in comparison with other carbon materials including: CN-BC[26], aPCN[36], PCNS-6[44], PCN/CNF[45], N, S-PCN[46], N-PMNC[47], FGN-300[48]

3 Conclusions

We have successfully synthesized free-standing interconnected N, S-codoped 3D carbon networks (a-NSC) with large SSA and hierarchical meso-microporous structure. This is achieved by the pyrolysis of bacterial cellulose@polyrhodanine derived from oxidation polymerization processes. These structural features not only provide a large ion-accessible surface area for ions adsorption, but also ensure efficient electron and ion transport along 3D directions. As a result, the prepared a-NSC exhibits a high specific capacitance of 340 F·g^{-1} at 0.5 A·g^{-1} in aqueous electrolyte with high-rate capability. Moreover, a symmetrical EDLCs device displays a short time constant of 0.35 s in 1 M $TEABF_4$/AN electrolyte, obtaining a maximum energy density of 32.1 W • h • kg^{-1} at a power density of 637 W • kg^{-1}. We believe that the in situ multi-heteroatoms doping can be extended to other carbon nanostructures (0D, 2D), achieved by using nanosphere or nanosheet precursors as polymerization templates. This versatile method enables biomass-derived porous carbon to exploit its immense potentials in energy storage applications.

Acknowledgements

This work was supported by the National Basic Research Program of China (973 Program) (No. 2014CB239701), the National Natural Science Foundation of China (Nos. 51672128, 51372116, 21773118), the Natural Science Foundation of Jiangsu Province (Nos. BK20150739, BK20151468), the Prospective Joint Research Project of Cooperative Innovation Fund of Jiangsu Province (No. BY2015003-7), and the Project Funded by the Priority Academic Program Development of Jiangsu Higher Education Institutions (PAPD).

References:

[1] FORSE A C, MERLET C, GRIFFIN J M, et al. New perspectives on the charging mechanisms of supercapacitors[J]. J Am Chem Soc, 2016, 138(18): 5731-5744.

[2] ZHANG F, LIU T, LI M, et al. Multiscale pore network boosts capacitance of carbon electrodes for ultrafast charging[J]. Nano Lett, 2017, 17(5): 3097-3104.

[3] WANG Y G, SONG Y, XIA Y Y. Electrochemical capacitors: mechanism, Materials, systems, characterization and applications[J]. Chem Soc Rev, 2016, 45:5925-5950.

[4] YU M, LIN D, FENG H, et al. Boosting the energy density of carbon-based aqueous supercapacitors by optimizing the surface charge[J]. Angew Chem Int Ed,2017, 56(20):5454-5459.

[5] XU Y, TAO Y, ZHENG X, et al. A metal-free supercapacitor electrode material with a record high volumetric capacitance over 800 F cm^{-3} [J]. Adv Mater,2016, 27(48):8082-8087.

[6] PENG L, PENG X, LIU B, et al. Ultrathin two-dimensional MnO_2/graphene hybrid nanostructures for high-performance flexible planar supercapacitors[J]. Nano Lett, 2013, 13(5):2151-2157.

[7] ZHONG C, DENG Y, HU W, et al. A review of electrolyte materials and compositions for electrochemical supercapacitors[J]. Chem Soc Rev, 2015, 44:7484-7539.

[8] WU Z, LI L, YAN J M, et al. Materials design and system construction for conventional and new-concept supercapacitors[J]. Adv Sci, 2017, 4(6): 1600382.

[9] ZHANG L, YANG X, ZHANG F, et al. Controlling the effective surface area and pore size distribution of sp^2 carbon materials and their impact on the capacitance performance of these materials[J]. J Am Chem Soc, 2013, 135(15):5921-5929.

[10] CANDELARIA S L, SHAO Y, ZHOU W, et al. Nanostructured carbon for energy storage and conversion[J]. Nano Energy,2012, 1(2):195-220.

[11] BÉGUIN F, PRESSER V, BALDUCCI A, et al. Carbons and electrolytes for advanced supercapacitors[J]. Adv Mater, 2014, 26(14): 2219-2251.

[12] XU Y, LIN Z, ZHONG X, et al. Holey graphene frameworks for highly efficient capacitive energy storage[J]. Nat Commun, 2014, 5:4554.

[13] YU Z, TETARD L, ZHAI L, et al. Supercapacitor electrode materials: Nanostructures from 0 to 3 dimensions[J]. Energy Environ Sci, 2015, 8:702-730.

[14] LONG C, QI D, WEI T, et al. Nitrogen-doped carbon networks for high energy density supercapacitors derived from polyaniline coated bacterial cellulose [J]. Adv Funct Mater 2014, 24(25):3953-3961.

[15] CHEN L F, HUANG Z H, LIANG H W, et al. Three-dimensional heteroatom-doped carbon nanofiber networks derived from bacterial cellulose for supercapacitors[J]. Adv Funct Mater, 2015, 24(32): 5104-5111.

[16] DUTTA S, KIM J, IDE Y, et al. 3D network of cellulose-based energy storage devices and related emerging applications[J]. Mater Horiz, 2017, 4: 522-545.

[17] CHEN L F, LU Y, YU L, et al. Designed formation of hollow particle-based nitrogen-doped carbon nanofibers for high-performance supercapacitors[J]. Energy Environ Sci, 2017,10:1777-1783.

[18] SHENG L, WEI T, LIANG Y, et al. Vertically oriented graphene nanoribbon fibers for high-volumetric energy density all-solid-state asymmetric supercapacitors[J]. Small, 2017, 13(22):1700371.

[19] SALUNKHE R R, KANETI Y V, KIM J, et al. Nanoarchitectures for metal-organic framework-de-

rived nanoporous carbons toward supercapacitor applications[J]. Acc Chem Res, 2016, 49(12):2796-2806.

[20] PAN Z, LIU M, YANG J, et al. High electroactive material loading on a carbon nanotube@3D graphene aerogel for high-performance flexible all-solid-state asymmetric supercapacitors[J]. Adv Funct Mater, 2017, 27(27):1701122.

[21] WANG J, NIE P, DING B, et al. Biomass derived carbon for energy storage devices[J]. J Mater Chem A, 2016, 5:2411-2428.

[22] XIN W, SONG Y, PENG J, et al. Synthesis of biomass-derived mesoporous carbon with super adsorption performance by an aqueous cooperative assemble route[J]. ACS Sustainable Chem Eng,2017, 5(3):2312-2319.

[23] LING Z, WANG Z, ZHANG M, et al. Sustainable synthesis and assembly of biomass-derived B/N co-doped carbon nanosheets with ultrahigh aspect ratio for high-performance supercapacitors[J]. Adv Funct Mater, 2016, 26(1):111-119.

[24] WU Z Y, LIANG H W, CHEN L F, et al. Bacterial cellulose: A robust platform for design of three dimensional carbon-based functional nanomaterials[J]. Acc Chem Res, 2016, 49(1):96-105.

[25] WANG X, KONG D, ZHANG Y, et al. All-biomaterial supercapacitor derived from bacterial cellulose [J]. Nanoscale, 2016, 8:9146-9150.

[26] HAO X D, WANG J, DING B, et al. Bacterial-cellulose-derived interconnected meso-microporous carbon nanofiber networks as binder-free electrodes for high-performance supercapacitors [J]. J Power Sources, 2017, 352:34-41.

[27] WANG J, KASKEL S. KOH activation of carbon-based materials for energy storage[J]. J Mater Chem, 2012, 22:23710-23725.

[28] CUI J, XI Y, CHEN S, et al. Prolifera-green-tide as sustainable source for carbonaceous aerogels with hierarchical pore to achieve multiple energy storage [J]. Adv Funct Mater, 2016, 26(46):8487-8495.

[29] ZHAO J, LAI H, LYU Z, et al. Hydrophilic hierarchical nitrogen-doped carbon nanocages for ultrahigh supercapacitive performance[J]. Adv Funct Mater, 2015, 27(23):3541-3545.

[30] LIN T, CHEN I W, LIU F, et al. Nitrogen-doped mesoporous carbon of extraordinary capacitance for electrochemical energy storage[J]. Science, 2015, 350(6267):1508-1513.

[31] LI X, HAO C, TANG B, et al. Supercapacitor electrode materials with hierarchically structured pores from carbonization of MWCNTs and ZIF-8 composites[J]. Nanoscale, 2017, 9:2178-2187.

[32] HASEGAWA G, DEGUCHI T, KANAMORI K, et al. High-level doping of nitrogen, phosphorus, and sulfur into activated carbon monoliths and their electrochemical capacitances[J]. Chem Mater, 2015, 27(13):4703-4712.

[33] PANG Q, TANG J, HUANG H, et al. A nitrogen and sulfur dual-doped carbon derived from polyrhodanine@cellulose for advanced lithium-sulfur batteries[J]. Adv Mater, 2015, 27(39):6021-6028.

[34] LIANG J, JIAO Y, JARONIEC M, et al. Sulfur and nitrogen dual-doped mesoporous graphene electrocatalyst for oxygen reduction with synergistically enhanced performance[J]. Angew Chem Int Ed, 2012, 51(46):11496-11500.

[35] WANG T, WANG L X, WU D L, et al. Interaction between nitrogen and sulfur in co-doped graphene and synergetic effect in supercapacitor[J]. Sci Rep, 2015, 5:9591.

[36] LI Y, WANG G, WEI T, et al. Nitrogen and sulfur co-doped porous carbon nanosheets derived from willow catkin for supercapacitors[J]. Nano Energy, 2016, 19:165-175.

[37] QU K, ZHENG Y, JIAO Y, et al. Polydopamine-inspired, dual heteroatom-doped carbon nanotubes for highly efficient overall water splitting[J]. Adv Energy Mater, 2016, 7(9):1602068.

[38] HAO X D, WANG J, DING B, et al. Nitrogen-doped porous carbon nanospheres from natural sepia ink: Easy preparation and extraordinary capacitive performance[J]. Chem Nano Mat, 2017, 3:895-901.

[39] LIU Y, ZHOU J, ZHU E, et al. Facile synthesis of bacterial cellulose fibres covalently intercalated with graphene oxide by one-step cross-linking for robust supercapacitors[J]. J Mater Chem C, 2015, 3:1011-1017.

[40] WANG J, DING B, HAO X D, et al. A modified molten-salt method to prepare graphene electrode with high capacitance and low self-discharge rate[J]. Carbon, 2016, 102:255-261.

[41] QU K, ZHENG Y, ZHANG, et al. Promotion of electrocatalytic hydrogen evolution reaction on nitrogen-doped carbon nanosheets with secondary heteroatoms[J]. ACS Nano, 2017, 11(7):7293-7300.

[42] HOU J, CAO C, IDREES F, et al. Hierarchical porous nitrogen-doped carbon nanosheets derived

from silk for ultrahigh-capacity battery anodes and supercapacitors[J]. ACS Nano, 2015, 9(3):2556-2564.

[43] WANG J, TANG J, DING B, et al. Hierarchical porous carbons with layer-by-layer motif architectures from confined soft-template self-assembly in layered materials [J]. Nat Commun, 2017, 8: 15717.

[44] WANG Y, DOU H, DING B, et al. Nanospace-confined synthesis of oriented porous carbon nanosheets for high-performance electrical double layer capacitors[J]. J Mater Chem A, 2016, 4:16879-16885.

[45] CHEN C, YU D, ZHAO G, et al. Three-dimensional scaffolding framework of porous carbon nanosheets derived from plant wastes for high-performance supercapacitors[J]. Nano Energy, 2016, 27: 377-389.

[46] JIANG Y, YAN J, WU X, et al. Facile synthesis of carbon nanofibers-bridged porous carbon nanosheets for high-performance supercapacitors[J]. J Power Sources, 2016, 307:190-198.

[47] PENG H, MA G, ZHANG Z, et al. Nitrogen-doped interconnected carbon nanosheets from pomelo mesocarps for high performance supercapacitors[J]. Electrochim Acta, 2016, 190:862-871.

[48] YAN J, WANG Q, WEI T, et al. Template-assisted low temperature synthesis of functionalized graphene for ultrahigh volumetric performance supercapacitors [J]. ACS Nano, 2014, 8(5):4720-4729.

Mr. **Zhu Jiajia** received his B. S. degree in applied chemistry from Yancheng Institute of Technology in 2010. He is currently a Ph. D. candidate under the supervision of Prof. Zhang Xiaogang at Nanjing University of Aeronautics and Astronautics. His research interests include supercapacitor and new energy materials.

Mr. **Hao Xiaodong** received his B. S. degree in applied chemistry in 2015 and M. S. degree in physical chemistry in 2018 from Nanjing University of Aeronautics and Astronautics (NUAA). His research focuses on advanced electrode materials for energy-storage devices, such as carbon and nanomaterials.

Dr. **Wang Jie** received her B. S. degree in chemistry from Huaiyin Normal University in 2011 and Ph. D. degree in materials physics and chemistry from NUAA in 2017, respectively. She is now working in National Institute for Materials Science as a Postdoctoral. Her current research is focused on advanced materials for electrochemical energy storage devices, such as carbon and nanomaterials.

Mr. **Guo Hongshuai** received his B. S. degree in applied chemistry 2016 from NUAA. He is currently pursuing his M. S. degree under the supervision of Prof. Zhang Xiaogang at NUAA. His research focuses on advanced electrode materials for energy-storage devices, such as supercapacitor.

Prof. **Dou Hui** received his Ph. D. degree from Chengdu Institute of Organic Chemistry, Chinese Academy of Sciences in 2003. She joined in NUAA in 2005, where she worked as an associate professor of nuclear science and engineering department in College of Material Science and Engineering. She is now a professor and her current research interests include new energy materials, green chemistry technology and nuclear waste disposal.

Prof. **Zhang Xiaogang** received his Ph. D. degree in chemistry from Lanzhou University in 2001. He joined in NUAA in 2005 as a professor of chemistry in College of Material Science and Engineering. He is now a Fellow of the Royal Society of Chemistry and the Director of the Jiangsu Key Laboratory of Materials and Technologies for Energy Conversion. His current research interests include the design and development of nanostructured composites and their applications in energy storage and conversion.

(Production Editor: Zhang Tong)

Supporting Information

Biomass-Derived Nitrogen and Sulfur Co-Doped 3D Carbon Networks with Interconnected Meso-Microporous Structure for High-Performance Supercapacitors

Zhu Jiajia, *Hao Xiaodong*, *Wang Jie*, *Guo Hongshuai*,
Dou Hui, *Zhang Xiaogang*

Jiangsu Key Laboratory of Electrochemical Energy Storage Technologies, College of Material Science and Engineering,
Nanjing University of Aeronautics and Astronautics, Nanjing 210016, P. R. China

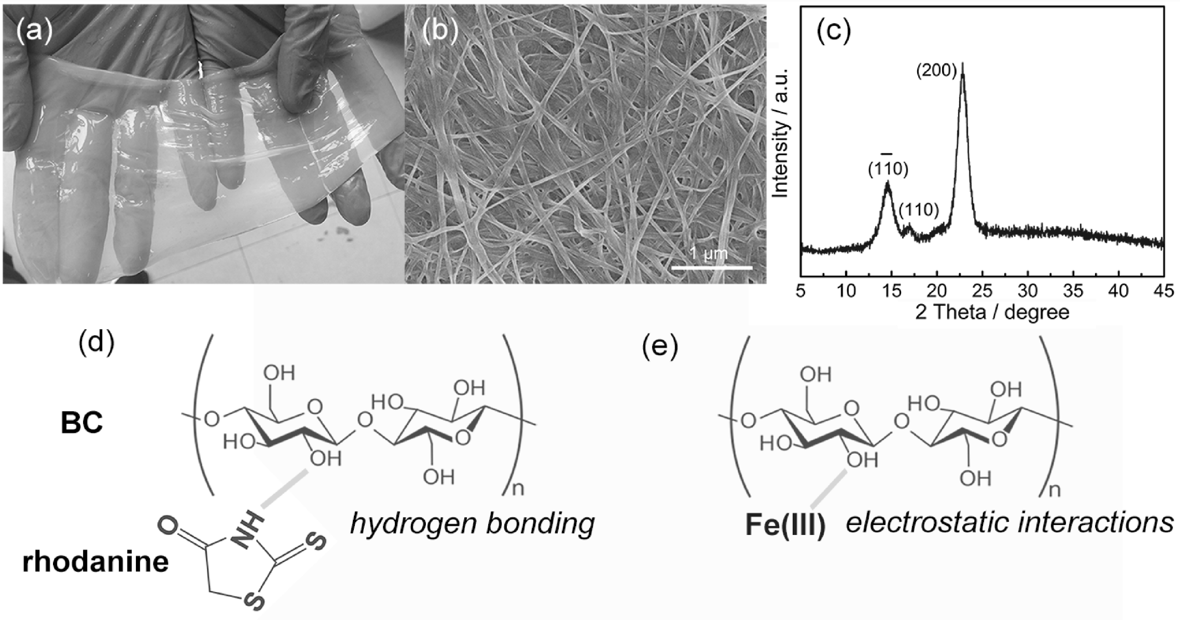

Fig. S1 (a) Digital photograph of BC pellicle. (b) SEM image and (c) XRD pattern of BC pellicle after freeze-drying. The schematic illustration of (d) hydrogen bonding and (e) electrostatic interactions

From the XRD pattern (Fig. S1c), bacterial cellulose (BC) shows a typical profile of cellulose I with three typical diffraction peaks occurring in the region of 10—25°. Besides, BC possesses abundant surface hydroxyl groups (—OH) along its networks with negatively charged sites, which can be determined by the FTIR spectra (Fig. S4).

The high proportion of activator will destroy the nanofiber morphology of NSC, thus the applicable mass ratio of KOH to NSC is 1∶1.

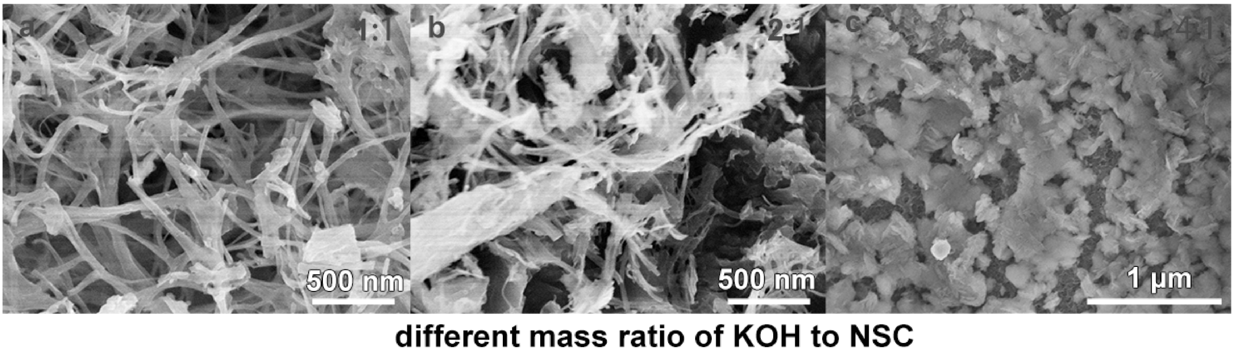

Fig. S2 SEM images of different mass ration of KOH to NSC: (a)1∶1, (b)2∶1, (c)4∶1.

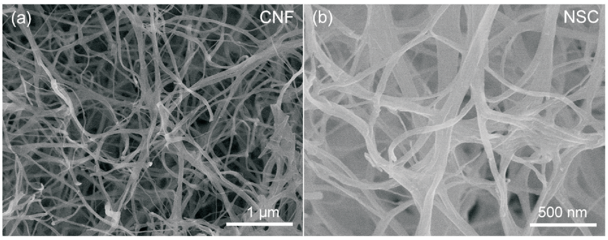

Fig. S3 SEM images of (a) CNF and (b) NSC

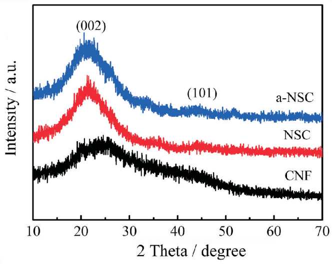

Fig. S4 (a) XRD patterns of CNF, NSC and a-NSC

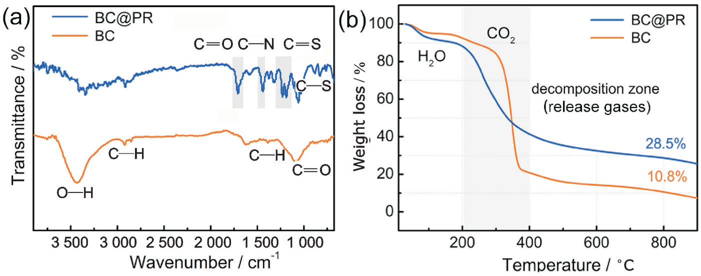

Fig. S5 (a) FTIR spectra and (b) TGA curves for BC and BC@PR pellicle

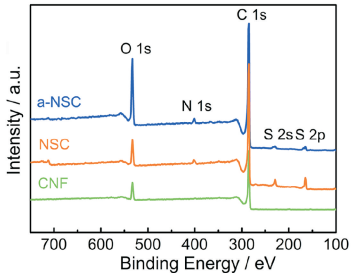

Fig. S6 XPS survey spectra of CNF, NSC and a-NSC

Table S1 The atomic percentages of C, N, S of different chemical states for a-NSC.

Samples	C═C/C—C	C—O	C═O	O—C═O	N—6	N—5	N—Q	N—O	C—S-C	SO$_x$
a-NSC	81.0%	11.6%	2.9%	4.5%	42.8%	13.6%	40.2%	3.4%	86%	14%

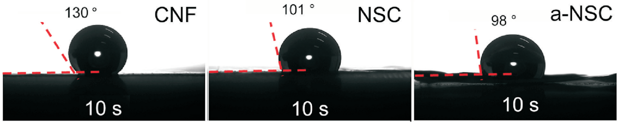

Fig. S7 The contact angle tests of different electrodes with 6 M KOH

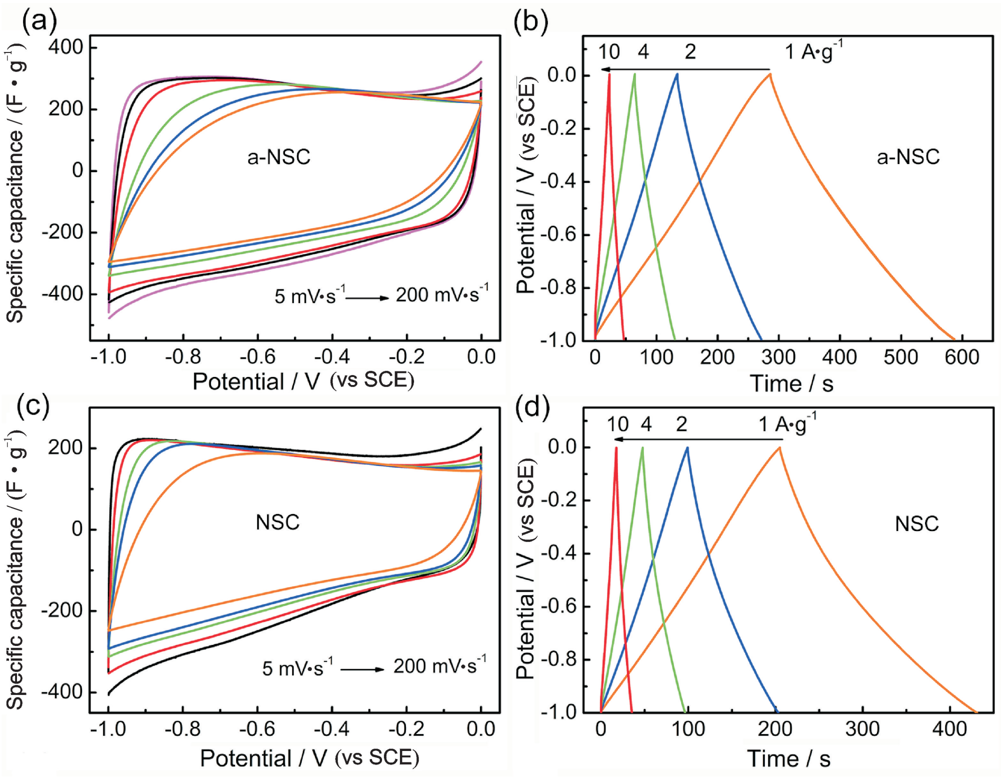

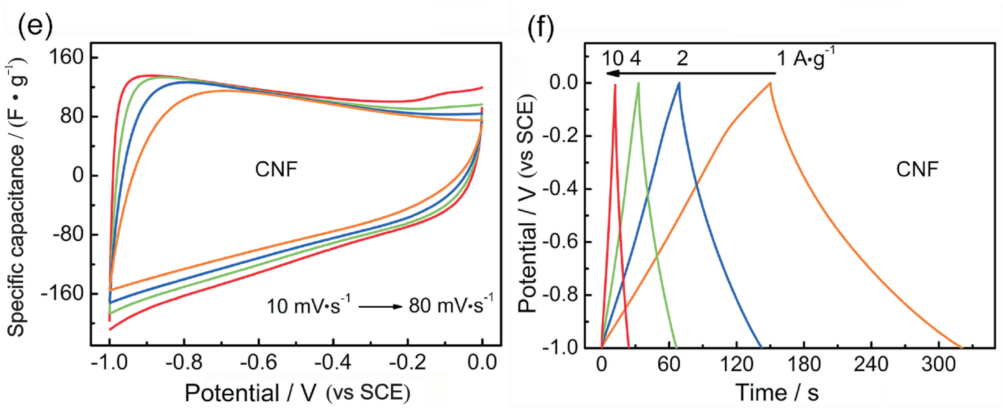

Fig. S8 CV plots of (a) a-NSC, (c) NSC and (e) CNF electrodes at different scan rates. GCD curves of (b) a-NSC, (d) NSC and (f) CNF electrodes at different current densities

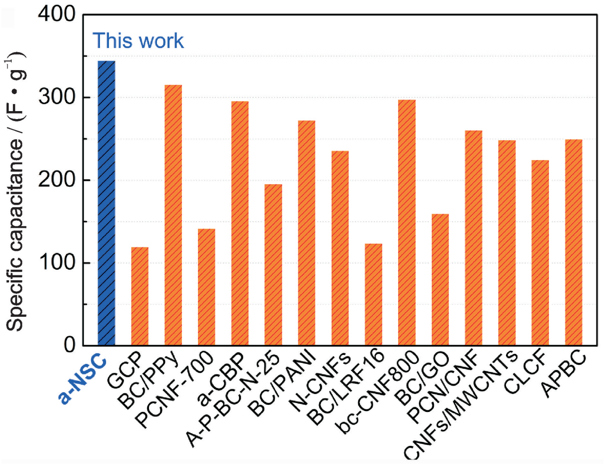

Fig. S9 Comparison of the capacitance of a-NSC electrode with other carbon materials derived from bacterial cellulose tested in aqueous electrolyte including: GCP[1], BC/PPy[2], PCNF-700[3], a-CBP[4], A-P-BC-N-25[5], BC/PANI[6], N-CNFs[7], BC/LRF16[8], bc-CNF800[9], BC/GO[10], PCN/CNF[11], CNFs/MWCNTs[12], CLCF[13], APBC[14]

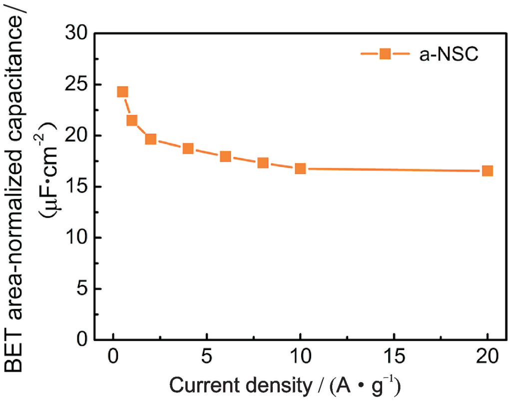

Fig. S10 The BET area-normalized capacitance of a-NSC

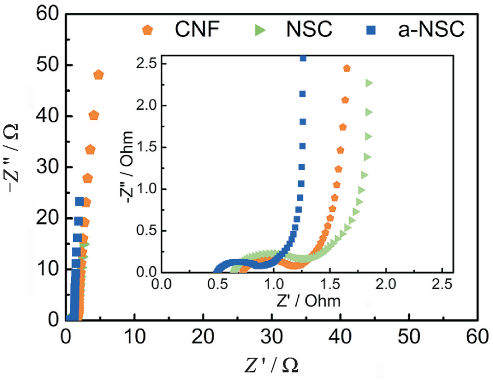

Fig. S11 Nyquist plots of a-NSC, NSC and CNF electrodes. Inset magnifies the high-frequency range

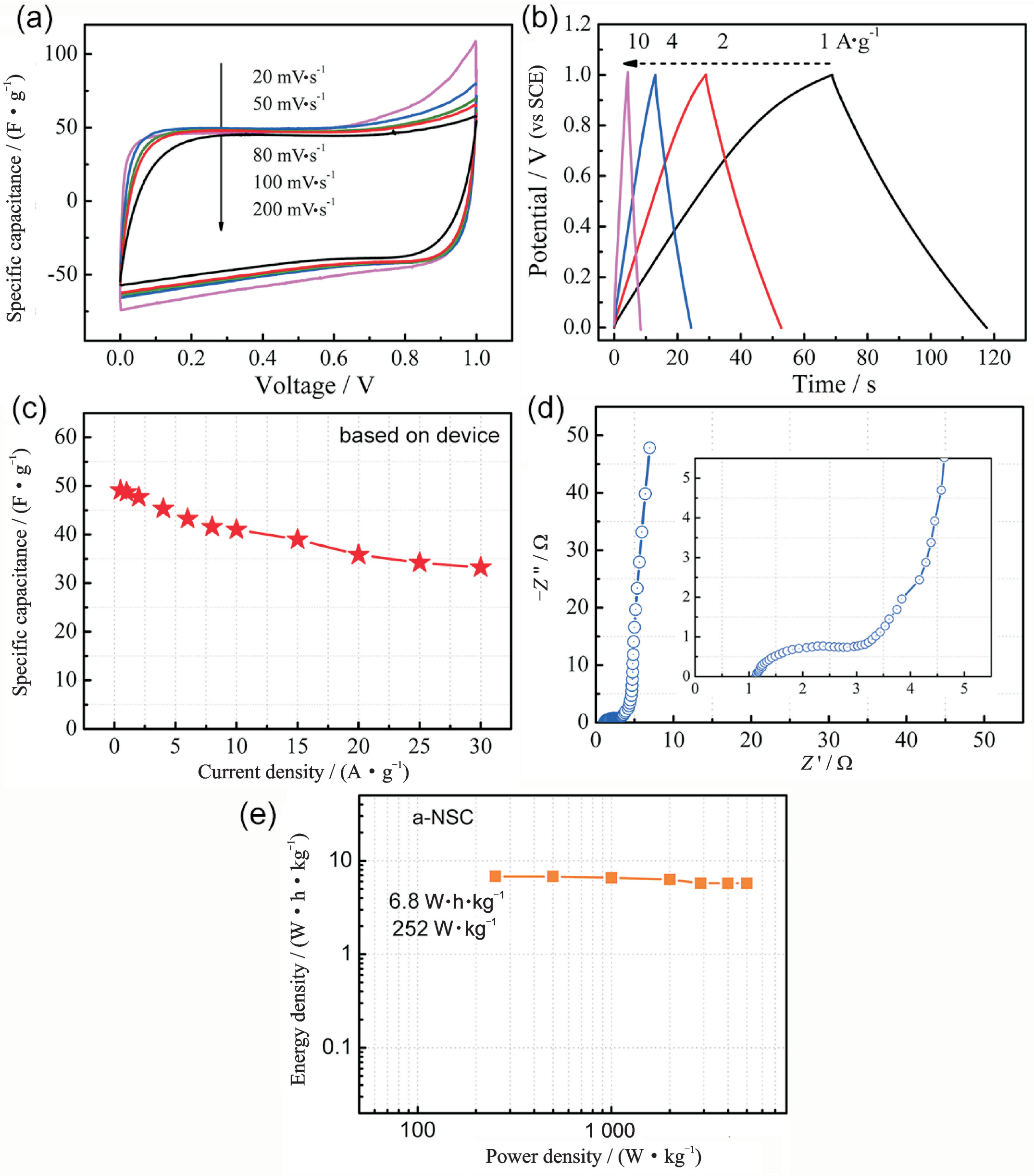

Fig. S12 Symmetrical supercapacitor performances of a-NSC using 6 M KOH as electrolyte. (a) CV plots. (b) GCD curves. (c) Specific capacitance vs current density. (d) Nyquist plot. (e) Ragone plot

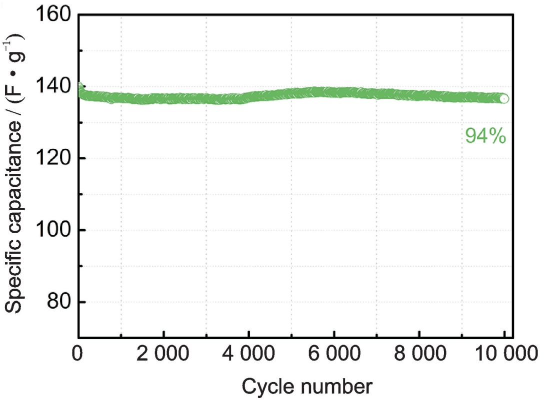

Fig. S13 Cycling stability of a-NSC at 2 A • g^{-1} using an organic electrolyte of $TEABF_4$/AN

Electrochemical Measurements

The BET area-normalized capacitance C_{SA} ($\mu F \cdot cm^{-2}$) was estimated from:

$$C_{SA} = \frac{C_s}{S_{BET}} \times 100$$

where S_{BET} is the specific surface area ($m^2 \cdot g^{-1}$) derived from the N_2 adsorption and C_S is the specific capacitance ($F \cdot g^{-1}$).

References:

[1] Weng Z, Su Y, Wang D W, et al. Graphene-Cellulose Paper Flexible Supercapacitors[J]. *Adv. Energy Mater.*, 2011, 1(5): 917-922.

[2] Wang H H, Bian L, Zhou P P, et al. Core-sheath structured bacterial cellulose/polypyrrole nanocomposites with excellent conductivity as supercapacitors [J]. *J. Mater. Chem. A*, 2012, 1: 578-584.

[3] Yuan D S, Huang X J, Yan J, et al. Porous Carbon Nanofibers Derived from Bacterial Cellulose for Sustainable Energy Storage [J]. *Sci. Adv. Mater.*, 2013, 5: 1694-1700.

[4.] Long C L, Qi D P, Wei T, et al. Nitrogen-Doped Carbon Networks for High Energy Density Supercapacitors Derived from Polyaniline Coated Bacterial Cellulose[J]. *Adv. Funct. Mater.*, 2014, 24(25): 3953-3961.

[5] Chen L F, Huang Z H, Liang H W, et al. Flexible all-solid-state high-power supercapacitor fabricated with nitrogen-doped carbon nanofiber electrode material derived from bacterial cellulose[J]. *Energy Environ. Sci.*, 2013, 6:3331-3338.

[6] Wang H H, Zhu E W, Yang J Z, et al. Bacterial Cellulose Nanofiber-Supported Polyaniline Nanocomposites with Flake-Shaped Morphology as Supercapacitor Electrodes[J]. *J. Phys. Chem. C*, 2012, 116(24): 13013-13019.

[7] Cai J, Niu H T, Li Z Y, et al. High-Performance Supercapacitor Electrode Materials from Cellulose-Derived Carbon Nanofibers[J]. *ACS Appl. Mater. Interfaces*, 2015, 7(27): 14946-14953.

[8] Xu X Z, Zhou J,. Nagaraju D H, et al. Flexible, Highly Graphitized Carbon Aerogels Based on Bacterial Cellulose/Lignin: Catalyst - Free Synthesis and its Application in Energy Storage Devices[J] *Adv. Funct. Mater.*, 2015, 25(21): 3193-3202.

[9] Liu Y, Lu T, Sun Z, et al. Ultra-thin carbon nanofiber networks derived from bacterial cellulose for capacitive deionization[J]. *J. Mater. Chem. A*, 2015, 3:8693-8700.

[10] Liu Y, Zhou J, Zhu E W, et al. Facile synthesis of bacterial cellulose fibres covalently intercalated with graphene oxide by one-step cross-linking for robust supercapacitors[J]. *J. Mater. Chem. C*, 2015, 3, 1011-1017.

[11] Jiang Y T, Yan J, Wu X L, et al. Facile synthesis of carbon nanofibers-bridged porous carbon nanosheets for high-performance supercapacitors[J]. *J. Power Sources*, 2016, 307: 190-198.

[12] Yang C, Li D G. Flexible and foldable supercapacitor electrodes from the porous 3D network of cellulose nanofibers, carbon nanotubes and polyaniline [J]. *Mater Lett*, 2015, 155: 78-81.

[13] Cheng Y L, Huang L, Xiao X, et al. Flexible and cross-linked N-doped carbon nanofiber network for high performance freestanding supercapacitor electrode[J]. *Nano Energy*, 2015, 15: 66-74.

[14] Wang X J, Kong D B, Zhang Y B, et al. All-biomaterial supercapacitor derived from bacterial cellulose [J]. *Nanoscale*, 2016, 8: 9146-9150.